THE UNIVERSITY of EDINBURGH

Edinburgh Research Explorer

Calibrating Lattice Boltzmann Flow Simulations and Estimating Uncertainty in the Permeability of Complex Porous Media

Citation for published version:
Hosa, A, Curtis, A & Wood, R 2016, 'Calibrating Lattice Boltzmann Flow Simulations and Estimating Uncertainty in the Permeability of Complex Porous Media: Lattice Boltzmann Flow Simulations and Estimating Uncertainty ', *Advances in Water Resources*, vol. 94, pp. 60-74.
https://doi.org/10.1016/j.advwatres.2016.04.020

Digital Object Identifier (DOI):
10.1016/j.advwatres.2016.04.020

Link:
Link to publication record in Edinburgh Research Explorer

Document Version:
Peer reviewed version

Published In:
Advances in Water Resources

Publisher Rights Statement:
© 2016 Elsevier Ltd. All rights reserved.

General rights
Copyright for the publications made accessible via the Edinburgh Research Explorer is retained by the author(s) and / or other copyright owners and it is a condition of accessing these publications that users recognise and abide by the legal requirements associated with these rights.

Take down policy
The University of Edinburgh has made every reasonable effort to ensure that Edinburgh Research Explorer content complies with UK legislation. If you believe that the public display of this file breaches copyright please contact openaccess@ed.ac.uk providing details, and we will remove access to the work immediately and investigate your claim.

OPEN ACCESS

Download date: 29. Apr. 2024

Calibrating Lattice Boltzmann Flow Simulations and Estimating Uncertainty in the Permeability of Complex Porous Media

Hosa, Aleksandra[a,b,*], Curtis, Andrew[a,b], Wood, Rachel[a,b]

[a] *School of GeoSciences, The University of Edinburgh, Grant Institute, The King's Buildings, James Hutton Road, Edinburgh EH9 3FE*
[b] *International Centre for Carbonate Reservoirs (ICCR)*

Abstract

A common way to simulate fluid flow in porous media is to use Lattice Boltzmann (LB) methods. Permeability predictions from such flow simulations are controlled by parameters whose settings must be calibrated in order to produce realistic modelling results. Herein we focus on the simplest and most commonly used implementation of the LB method: the single-relaxation-time BGK model. A key parameter in the BGK model is the relaxation time τ which controls flow velocity and has a substantial influence on the permeability calculation. Currently there is no rigorous scheme to calibrate its value for models of real media. We show that the standard method of calibration, by matching the flow profile of the analytic Hagen-Poiseuille pipe-flow model, results in a BGK-LB model that is unable to accurately predict permeability even in simple realistic porous media (herein, Fontainebleau sandstone). In order to reconcile the differences between predicted permeability and experimental data, we propose a method to calibrate τ using an enhanced Transitional Markov Chain Monte Carlo method, which is suitable for parallel computer architectures. We also propose a porosity-dependent τ calibration that provides an excellent fit to experimental data and which creates an empirical model that can be used to choose τ for new samples of known porosity. Our Bayesian framework thus provides robust predictions

*Hosa, Aleksandra
Email address: ola.hosa@ed.ac.uk (Hosa, Aleksandra)

of permeability of realistic porous media, herein demonstrated on the BGK-LB model, and should therefore replace the standard pipe-flow based methods of calibration for more complex media. The calibration methodology can also be extended to more advanced LB methods.

Keywords: Uncertainty Quantification, Porous Media, Permeability, BGK Lattice Boltzmann, Fluid Flow, Bayesian

1. Introduction

Lattice Boltzmann (LB) simulation is one of the main methods used to predict flow through porous materials [1, 2, 3, 4]. Such simulations are often used to estimate particular quantities of interest concerning either the fluid flow or the porous medium. Amongst the most interesting flow properties in reservoir engineering (our current area of focus) is the permeability of porous subsurface rocks that contain fluid, and estimating permeability is important in a wide variety of other fields such as biology [5, 6, 7], medicine [8, 9], soil science [10, 11] and material science [12, 13, 14, 15].

The LB method simulates fluid flow by using the Boltzmann equation to dynamically update the fluid density as described by a set of interacting particles. The method relies on several parameters, some physics-based and some algorithmic, which must be calibrated before using LB to predict quantities of interest. The calibration of LB models has commonly been achieved by comparing the velocity of fluid flow simulated through a specific pore shape to one predicted analytically by the Hagen-Poiseuille equation [16]. The LB parameters are chosen to minimise the discrepancy of the flow profile that develops in specific pore sizes to corresponding theoretically predicted values. The deficiency of that method is that in real media the permeabilities to be matched by LB come from laboratory experiments and the above theoretical value does not include any experimental uncertainty, nor does it necessarily relate to real pore geometries which often contain a distribution of pore shapes and sizes with complicated network connectivity.

This paper provides a more robust method to predict permeability in real porous media using LB. Our quantity of interest is the permeability of natural, complex porous media, and we show that the standard practice of calibrating LB to theoretical predictions for even an idealised, simple system results in significant uncertainties and model deficiencies. It appears that there has never been a thorough uncertainty quantification of the predictive accuracy of LB. We therefore perform a Bayesian calibration of the physical LB parameters as well as the model insufficiency parameters, using real permeability data in place of the standard theoretical velocities in an analytical pipe model. Our method of calibration is shown to provide more accurate simulations than the standard method for the real pore systems studied.

Herein we present a calibration framework for the most basic LB model that uses the Bhatnagar-Gross-Krook (BGK) collision model. It is known that the prediction of permeability using this single-relaxation-time LB model is sensitive to parameter τ. This is due to insufficient consideration of the boundary conditions [17, 16], as the bounce-back boundary rule imposes the location of the solid boundary which has a numerical error that depends on the parameter τ. Multiple-relaxation-time (MRT) or two-relaxation-time (TRT) LB models [18, 19, 20] considerably reduce the dependence on parameter τ, but do not eliminate it completely [17, 16]. We confirm the dependence of permeability on τ in flow simulations in natural porous media using the BGK-LB model. Rather than performing purely a model-based sensitivity study where the variability in the predictions based on the variation of the fluid viscosity via its numerical parameter τ would be investigated, we assume a data-driven approach by using the full Bayesian framework. In further work we could apply the methodology developed here to the more complex TRT or MTR LB models.

We adopt a Bayesian framework for complex mechanical systems [21, 22, 23, 24, 25, 26, 27] to quantify and calibrate these parametric uncertainties based on experimental measurements of the pore size distribution in real samples and permeability measured in the same samples. Furthermore we propagate these uncertainties through LB simulations to make robust predictions of the relevant

quantity of interest. We employ an enhanced parallel variant of the Transitional Markov Chain Monte Carlo (TMCMC) algorithm [28, 29] to distribute the large number of LB runs in clusters with heterogeneous computer architectures [30]. TMCMC is a parallel evolutionary sampling algorithm inspired by particle filtering that involves annealing and local Monte Carlo steps. Our results demonstrate the value of the Bayesian framework for LB simulations and provide credible uncertainty intervals for their predictions. We thus demonstrate that permeability predictions using current methods may suffer from significant, unquantified and unaccounted for uncertainties. We propose a semi-empirical way to calibrate BGK-LB parameters more robustly in future.

The paper is organised as follows: in Section 2 we outline the elements of LB simulation. Section 3 describes the real porous medium used, in this case a Fontainebleau sandstone. Section 4 presents a Bayesian framework in the context of our experimental and computational set-up. Results for the Bayesian calibration of LB parameters are given in Section 5. In Section 6 we elaborate on the significance of our results compared to existing methods and on the implications for the future use of LB. Our summary and conclusions are presented in Section 7.

2. Lattice Boltzmann (LB)

LB methods are a popular way to simulate fluid flow [1, 2, 3, 4, 31] in many areas including material science [15, 14], hydrology [11], biology [9] as well as the simulation of oil and gas behaviour in porous rock [32, 33, 34, 35, 36]. LB simulations of flow through pore geometries derived from real rocks have been used to estimate effective permeability [37] or relative permeability [38, 39], using microporous rocks [40], sandstones [41] (even the same Fontainebleau sandstone that we use in this study [42]) and (typically with more complex porosity) carbonates [39]. Ever since computational power became sufficient to run LB on realistic simulations, this method has been a popular alternative to the direct solution of the Stokes equation. This is particularly true for complex, multi-scale media:

direct numerical simulations using gridded methods require extremely refined grids to capture the small scale complexities and the definition of boundary conditions becomes cumbersome due to the complexity of the geometry, both of which lead to high computational cost of simulation.

LB methods represent the fluid as a large number of particles, and calculates the probability (density) of finding a given particle at a given position on a discrete lattice mesh. The algorithm consists of two steps: advection and collision. In the advection step the particles are propagated along their velocity vectors to adjacent lattice sites. In collision, the particles converging at each lattice site interact: they collide and are redistributed according to their velocities as follows. First the density ρ and the velocity vector u of the fluid at all points in the lattice are calculated. Then the average velocity and force terms are calculated and the equilibrium densities for each velocity vector are found. Finally collision takes place in which the particle densities are adjusted through the fundamental equation of the BGK-LB model [43]:

$$f_i(x + v_i\Delta t, t + \Delta t) = f_i(x, t) - \frac{1}{\tau}(f_i(x, t) - f_i^{eq}(x, t)) \tag{1}$$

where i denotes the direction of momentum, f_i is the directional density (probability density function (PDF) per unit space of a particle traveling in direction i), f_i^{eq} is the equilibrium PDF, t is simulation time, Δt is the simulation time step, x is the location of the particle in the lattice, v_i is the velocity of the particle in direction i, and τ is the relaxation time parameter that is related to kinematic viscosity ν through the relation [44]

$$\nu = \frac{\tau - 0.5}{3} \tag{2}$$

Although τ is linked to kinematic viscosity (Equation (2)) and thus may seem to be a model state, it is in fact a model parameter. Due to numerical stability issues, the value of τ which directly corresponds to the viscosity of the fluid of interest (e.g. water) cannot be used and a value for which computation is stable is used instead [16]. Equation (2) then calculates permeability.

We perform LB simulations using the publicly available code LB3D v7.0, developed at University College London, University of Stuttgart and Eindhoven University of Technology [44]. After Narvaez et al. [16] we use a computational domain composed of inlet (I), outlet (O) and the sample of interest (S), with a periodic boundary condition imposed on the inlet and outlet sides of the domain and bounce-back boundaries on the remaining sides (Figure 1). We investigate four cases of single phase flow: in Case 1 we aim to calibrate relaxation parameter τ to the Hagen-Poiseuille (HP) law using our Bayesian framework and the same simulation set-up as Narvaez et al. [16] with pipe axes aligned in the z direction and varied widths $w = \{3, 4, 5, 6, 7, 12\}$. Domain dimensions in Figure 1 are defined as follows: $L_x = L_y = w + 2, L_S = 4w$, and $L_I = L_O = 3$. Case 2 takes into account the contribution of pores of different sizes to total error.

Cases 3 and 4 involve simulating flow through real rocks and calibration using real permeability data. In these cases we run the simulation on digital representations of cubic rock samples of dimension 100^3 lattice units (i.e. $L_x = L_y = L_S = 100$). We introduce inlet and outlet buffers of thickness $L_I = L_O = 10$, and forcing at the inlet cross section $C(1)$ (Figure 1). To avoid boundary issues we define the walls of the simulation domain that are parallel to the forcing direction to be solid. In each case we run LB simulations for 100000 time steps, at which point the properties of the simulations required to calculate permeability (velocity, density and pressure) become stable (Figure 3).

The permeability κ is calculated using Darcy's law:

$$\kappa = -\eta \frac{\langle v_z \rangle_S}{\langle \nabla p_z \rangle_{P \cap S}} \tag{3}$$

where η is the dynamic viscosity, $\langle v_z \rangle_S$ is an average over the sample S of the components of the fluid velocity parallel to the overall flow direction, and $\langle \nabla p_z \rangle_{P \cap S}$ is the pressure gradient in the pore space P of sample S in the direction of the flow. The dynamic viscosity is $\eta = \nu \langle \rho \rangle_{P \cap S}$, where ν is as defined in Equation (2), and P is the set of pore grid points of the simulation domain,

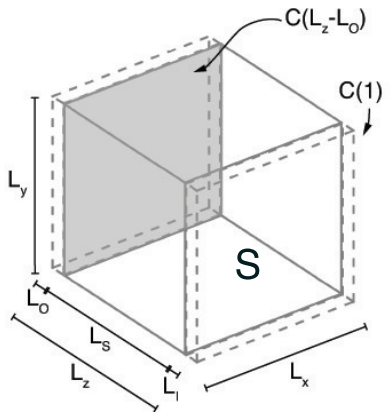

Figure 1: The computational domain of dimensions L_x, L_y and L_z consisting of the sample S (solid outline) of thickness L_S and inlet and outlet buffers (dashed outline) of thickness L_I and L_O. The buffers are introduced to avoid artefacts. The fluid is accelerated in the acceleration zone using body forces at the inlet cross section $C(1)$.

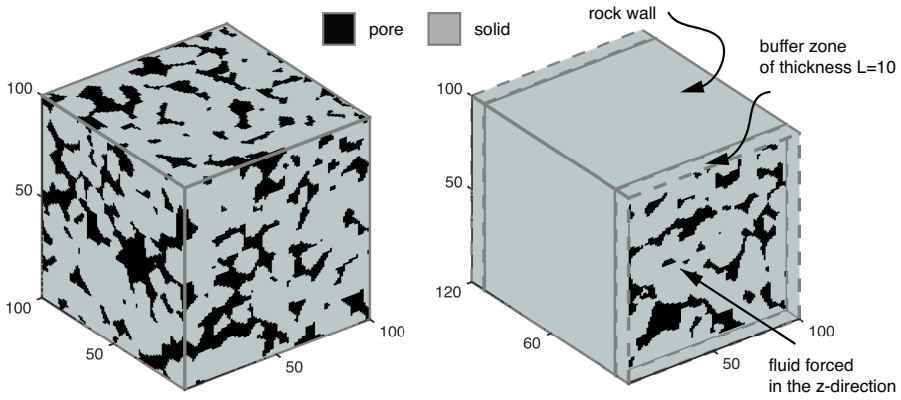

Figure 2: The computational domain in Cases 3 and 4. The Fontainebleau sandstone sample of dimensions 100^3 has buffer zones of thickness 10 attached to both walls perpendicular to the z-direction. The walls parallel to the fluid forcing direction are defined to be solid rock. The fluid is accelerated in the first layer ($z = 1$) of the inlet buffer.

and $\langle \rho \rangle_{P \cap S}$ is the average density of the fluid in the volume of the pore space of the sample.

Following Narvaez et. al [16] we make an approximation of the average fluid density using just two cross sections through the sample. This is justified by the fact that after a long simulation the values of density fall uniformly across the pores of the sample. We use an average of the values in the inlet cross section

$C(L_I + 1)$ and the outlet cross section $C(L_z - L_O)$, so:

$$\langle \rho \rangle_{IO} \approx \frac{\langle \rho \rangle_{C(L_z - L_O) \cap P} + \langle \rho \rangle_{C(L_I + 1) \cap P}}{2} \tag{4}$$

where we define $IO = (C(L_z - L_O) \cup C(L_I + 1)) \cap P$ which is the pore space in the inlet and outlet cross-sections. Similarly, the average pressure drop across the sample is approximated using the same two cross sections:

$$\langle \nabla p_z \rangle_{IO} \approx \frac{\langle p_z \rangle_{C(L_z - L_O) \cap P} - \langle p_z \rangle_{C(L_I + 1) \cap P}}{(L_S - 1)} \tag{5}$$

Due to the fact that the velocity of fluid varies inside the sample and depends on pore geometry and topology, we calculate average velocity $\langle v_z \rangle_S$ by dividing the sum of all velocity components in the direction of the flow across the entire sample S by the volume of the sample.

3. Porous media

The porous medium we use for Cases 3 and 4 is derived from 3D micro computed tomography (microCT) of a sample of Fontainebleau sandstone obtained at the Institute for Computational Physics of the University of Stuttgart (http://www.icp.uni-stuttgart.de/microct/) [45]. We use a 100^3 sub-image of the full image with voxel resolution of $14.6 \mu m$.

Since the microCT images are monochromatic (in this case their voxel values are within a range between 0 and 216) as illustrated in Figure 4, we must binarise the images into either solid or void before we can use them for LB simulations. Binarisation defines all voxels with monochromatic value less than a threshold to be pore space or void, and the rest to be solid. Figure 4 illustrates how choosing a higher threshold value results in a higher porosity sample than a lower threshold.

In our calibration method we investigate the porosity-permeability curve, so we need several samples of varied porosity. To obtain these we binarise the microCT image using eight different thresholds (6, 36, 66, 96, 126, 156, 186

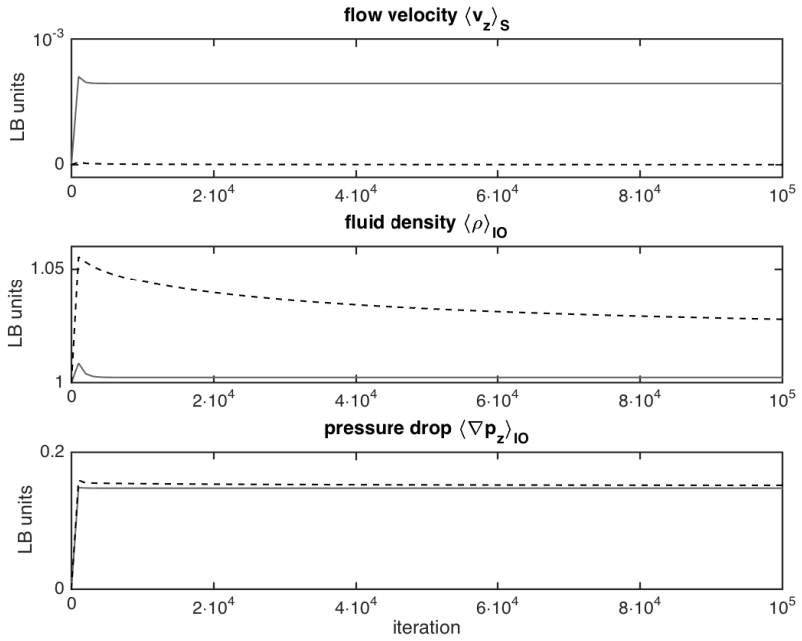

Figure 3: Outputs of the LB simulation used to calculate permeability shown throughout the run with $\tau = 0.6$ (100000 iterations): solid - high porosity (21.2%) sample, dashed - low porosity (6.2%) sample. From top to bottom we have average flow velocity in the direction of fluid forcing averaged over the volume of the entire sample - $\langle v_z \rangle_S$, the approximated average fluid density in the pores of the sample calculated using the inlet and outlet cross sections - $\langle \rho \rangle_{IO}$, and pressure difference between the inlet and outlet walls of the sample - $\langle \nabla p_z \rangle_{IO}$. All outputs are in dimensionless LB units.

and 216) to arrive at binarised representations with different porosities (6.2, 8.3, 9.8, 11.2, 12.7, 14.4, 16.4 and 21.2 percent, respectively). Figure 5 depicts these results, and Figure 6 illustrates that the corresponding porous media are complex and multiscaled as pore sizes range over an order of magnitude in all cases.

We are aware that the way we obtain samples of varying porosity by changing the binary threshold is not equivalent to obtaining samples in which differences in porosity arise from different stages of natural processes (i.e. diagenesis). However, the process of binarisation at different thresholds implemented here can be considered as a proxy for cementation. Greyscale values in the image change gradually from a grain (white, maximum pixel value of 216) to a pore

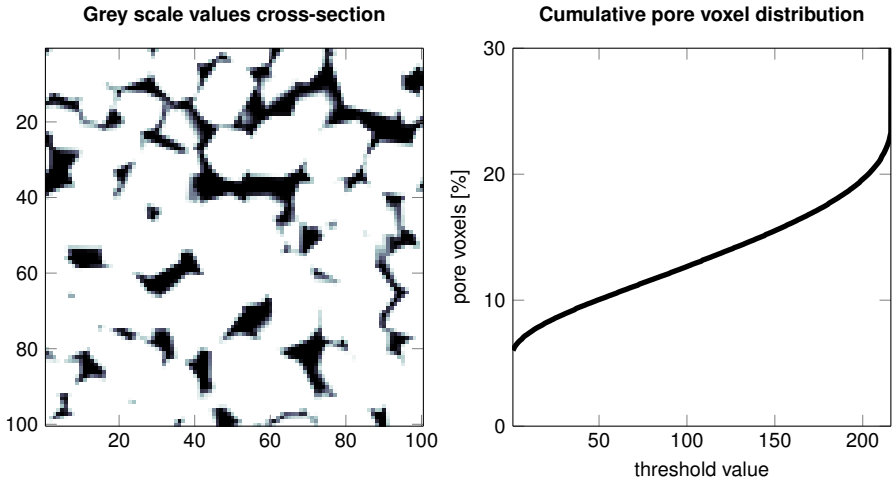

Figure 4: Slice through microCT image of Fontainebleau sandstone in grey scale (left). Cumulative percentage of pore voxels in a 3D sample of size 100^3 (right): the smaller the threshold we choose for binarisation (x-axis), the smaller the proportion of pore-voxels in the binarised medium (proportion of voxels on y-axis is equivalent to resultant porosity).

(black, minimum pixel value of 0), therefore as the binarisation threshold is decreased the grains are progressively being 'overgrown' with more solid voxels (a proxy for cement). This results in overall porosity of the rock decreasing with the threshold of binarisation, e.g. threshold of 186 results in a porosity of about 17%, while threshold of 156 results in more 'cement' overgrown around the grains and a porosity of 15% (Figure 4). In this way the samples binarised at different thresholds maintain topologies similar to samples of Fontainebleau sandstone at different porosities.

4. Bayesian framework

We now present an overview of the Bayesian framework for model-based uncertainty quantification that we use herein. We start with the general formulation and continue with case-specific adaptations. Table 1 contains a summary of all variables.

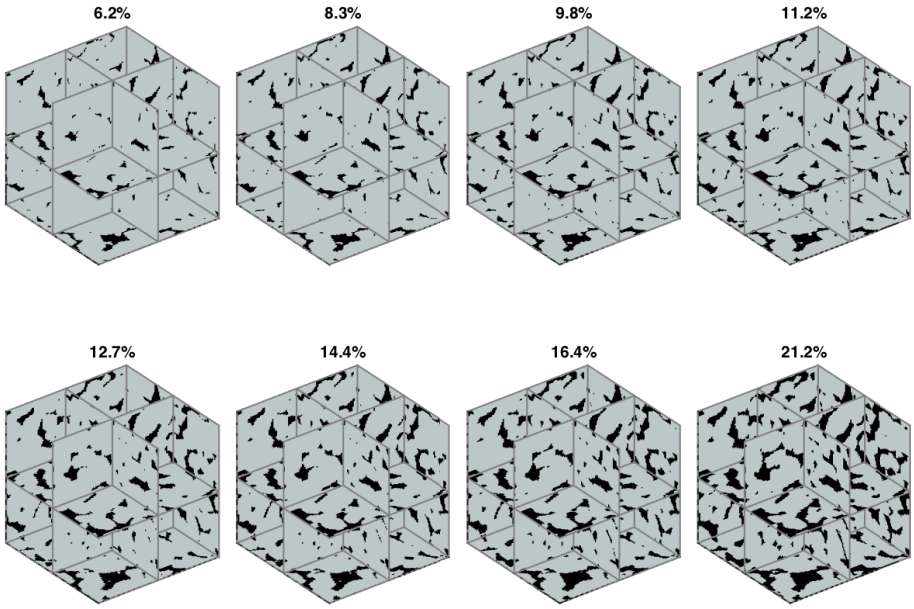

Figure 5: Slices through 3D microCT images of Fontainebleau sandstone of dimension 100^3 and resolution $14.6\mu m$. The same sample binarised at eight different thresholds creates samples with eight different porosities: 6.2, 8.3, 9.8, 11.2, 12.7, 14.4, 16.4 and 21.2 percent. Dark indicates pore space and light grey indicates solid.

4.1. General Bayesian formulation

Consider a class of models M which in our case will be the set of all LB models considered. Individual models within that class are assumed to differ due to variations in a set of parameters $\underline{\theta}$. Our goal is to use both data from empirical laboratory experiments or analytical calculations, and any other information available that is independent of the data (so-called *prior* information), to constrain appropriate values for $\underline{\theta}$.

In a Bayesian framework [47, 48], the uncertainty in parameters $\underline{\theta}$ of model class M is quantified with a prior probability distribution function (PDF) $\pi(\underline{\theta}|M)$ which is updated with information from data $\underline{D}$ to give the so-called *posterior*

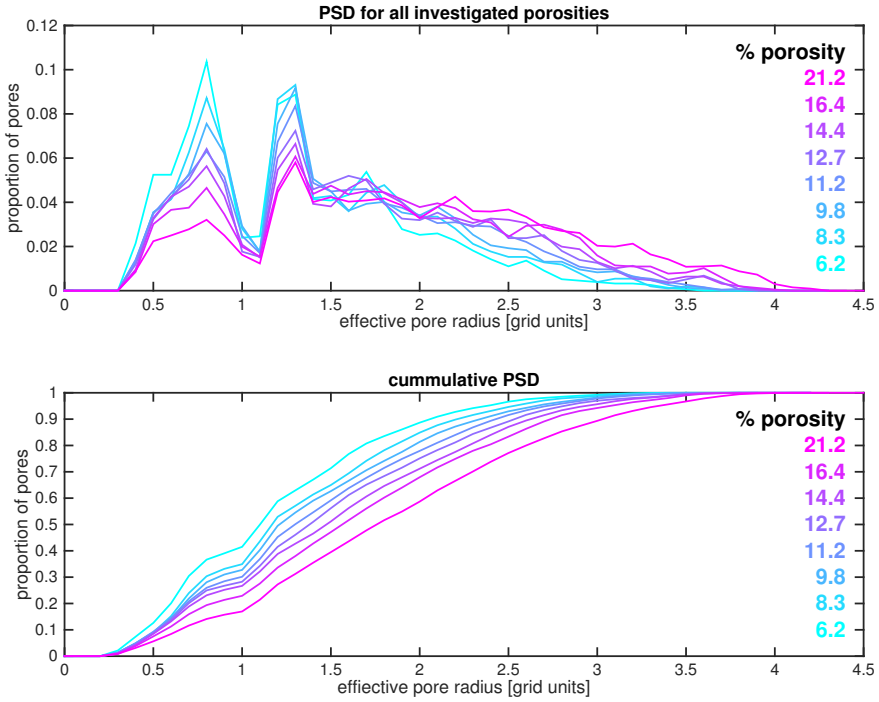

Figure 6: Effective pore size distribution (PSD) functions (top) and their cumulative distributions (bottom) for the microCT image of Fontainebleau sandstone binarised at eight different threshold values. The effective pore diameters, defined as the maximum diameter of a sphere that fits inside the pore, were calculated using the methods described in [46].

PDF $p(\underline{\theta}|\underline{D}, M)$ according to Bayes rule:

$$p(\underline{\theta}|\underline{D}, M) = \frac{p(\underline{D}|\underline{\theta}, M)\ \pi(\underline{\theta}|M)}{p(\underline{D}|M)} \tag{6}$$

Here $p(\underline{D}|\underline{\theta}, M)$ is the *likelihood* of observing data $\underline{D}$ within the model class considered given a particular set of parameter values $\underline{\theta}$, and $p(\underline{D}|M)$ is the so-called *evidence* or estimate for the model class as a whole being appropriate to represent data $\underline{D}$. This evidence is given by the multi-dimensional marginal integral of the numerator over the space of all possible LB model parameter values:

$$p(\underline{D}|M) = \int_{\underline{\theta}} p(\underline{D}|\underline{\theta}, M)\pi(\underline{\theta}|M)d\underline{\theta} \tag{7}$$

The prior PDF $\pi(\underline{\theta}|M)$ of the model parameters incorporates all available

Table 1: Variables used in the Bayesian formulation.

General formulation

$\underline{\theta}$	Model parameter set
M	LB model class
$\pi(\cdot)$	Prior PDF
$p(\cdot)$	Posterior PDF
$\underline{D}$	Measured data
$\underline{f}$	Model predictions
$\underline{e}$	Prediction error
n	Number of observations (measurements)
$J(\cdot)$	Weighted measure of fit between the model predictions and measured data
Σ	Covariance matrix of the error term
Q	Quantity of interest
N	Number of TMCMC samples

Case-specific formulation

$\underline{\theta} \equiv \tau$	LB model temporal relaxation parameter
$Q \equiv \kappa$	Permeability (κ) is the quantity of interest in all cases
$\underline{f_\kappa}$	Model predictions: permeability predicted in LB simulation
$\underline{D_{\kappa,A}}$	Measured data: analytically obtained permeability of a pipe of square cross-section in Cases 1 and 2
$\underline{D_{\kappa,E}}$	Measured data: experimentally derived permeability of Fontainebleau sandstone in Cases 3 and 4
w	Pipe width (size) in Case 2
σ_w^2	Variance of uncertainty on pore size w in Case 2
$g(w)$	Functional form of the weight variance in Case 2
$d(w)$	Pore size distribution in Case 2
ϕ	Porosity

information on the uncertainty of the model parameters before data $\underline{D}$ is taken into consideration. This may derive from previous experience in other modelling exercises, from mathematical knowledge (of convergence criteria of underlying equations, for example), or from any other relevant source. It could be obtained and parametrised by expert elicitation [49, 50], by literature surveys, or by conducting independent modelling tests.

Assuming that the model predictions $\underline{f}(\underline{\theta}|M)$ and the measurement data $\underline{D}$ satisfy the model prediction equation

$$\underline{D} = \underline{f}(\underline{\theta}|M) + \underline{e} \tag{8}$$

where the prediction error $\underline{e}$ (accounting for measurement, computational and modelling inadequacy) is normally distributed with zero mean and covariance matrix Σ, the likelihood $p(D|\underline{\theta}, M)$ is given as [21]

$$p(\underline{D}|\underline{\theta}, M) = \frac{|\Sigma(\underline{\theta})|^{-1/2}}{(2\pi)^{n/2}} \exp\left[-\frac{1}{2} J(\underline{\theta}; M)\right] \tag{9}$$

where

$$J(\underline{\theta}; M) = [\underline{D} - \underline{f}(\underline{\theta}|M)]^T \Sigma^{-1}(\underline{\theta})[\underline{D} - \underline{f}(\underline{\theta}|M)] \tag{10}$$

is the weighted measure of fit between the system model predictions and the measured data, $|\cdot|$ denotes determinant, and the parameter set $\underline{\theta}$ is augmented to include parameters that can be used to describe values of the covariance matrix Σ.

One of the key parameters to be identified within a BGK-LB simulation is the relaxation rate τ in Equation (1). In this work we concentrate on calibrating that parameter in four ways: Cases 1 and 2 use the Hagen-Poiseuille law, where data $\underline{D}$ is the analytically derived permeability $\underline{D_{\kappa,A}}$ in a pipe of square cross-section; Cases 3 and 4 both use experimental permeability data for Fontainebleau sandstone $\underline{D_{\kappa,E}}$, the distinction between them being that Case 3 is porosity-independent and Case 4 is porosity-dependent.

4.2. Bayesian formulation for calibration using Hagen-Poiseuille (HP) law (Cases 1 and 2)

When calibrating BGK-LB models using the Hagen-Poiseuille law we follow the steps of Narvaez et al. [16] and simulate the flow in a single open-ended pore of square cross-section (a pipe). We perform six LB simulations for pipes of various widths (3, 4, 5, 6, 7 and 12 lattice units). These widths are within the range of the pore widths typical for Fontainebleau sandstone. Figure 6 shows that the pore diameters range from 1 to 9 grid units for all investigated porosities. In each case the permeability derived from LB is compared with the analytically obtained permeability in a pipe of square cross-section calculated using the Hagen-Poiseuille law [16]:

$$\underline{D_{\kappa,A}}(w) = \lim_{m\to\infty} \frac{w^2}{4}\left(\frac{1}{3} - \frac{64}{\pi^5}\sum_{n=0}^{m}\frac{tanh\left((2n+1)\frac{\pi}{2}\right)}{(2n+1)^5}\right) \tag{11}$$

In this calibration we treat the pore size w as a model state rather than a model parameter. In this case the prediction error equation (8) which quantifies the discrepancy between the LB predictions of the permeability for each state w has the functional form $\underline{f}(\underline{\theta}|M) \equiv \underline{f_\kappa}(\tau; w)$ and the theoretically calculated values $\underline{D} \equiv \underline{D_{\kappa,A}}$ are given by

$$\underline{D_{\kappa,A}} = \underline{f_\kappa}(\tau; w) + \underline{e} \tag{12}$$

where $e \sim N(0, \sigma_w^2)$ and the variance of the error is some function $\sigma_w^2 = g(w)$ of the width w of the pipe.

In general we identify three separate possible sources of uncertainty within the term $\underline{e}$: experimental uncertainty σ_{exp}^2, sampling uncertainty $\sigma_{time-sample}^2$ and model error σ_{model}^2. The overall uncertainty associated with each size w of the pore [47] is then

$$\sigma_w^2 = \sigma_{exp}^2 + \sigma_{time-sample}^2 + \sigma_{model}^2 \tag{13}$$

Recall that the values $\underline{D_{\kappa,A}}$ as dictated from Hagen-Poiseuille flow are an-

alytically derived. Thus, in cases 1 and 2 there is no error associated with experimental measurements ($\sigma^2_{exp} = 0$). Furthermore, the sampling uncertainty in the case of LB is negligible, as the model reaches a steady equilibrium with minute fluctuations at steady state after $O(10^5)$ steps. This can be viewed in Figure 3 which shows the convergence of the system properties throughout a typical LB run. Hence $\sigma^2_{time-sample} \simeq 0$.

However, there is uncertainty associated with the inadequacy of the class M of BGK Lattice Boltzmann models to capture the theoretical values accurately (as LB is only a computational model). As a result of the first 2 components being negligible, the overall error for each width of the pipe σ^2_w is the model error, that is $\sigma^2_w \simeq \sigma^2_{model}$.

We investigate 2 ways of calculating the model error. The more straightforward (Case 1) treats all six considered pore sizes (3, 4, 5, 6, 7 and 12) equally, and the error is described with the formula:

$$\sigma^2_w = g(w) = \frac{1}{6}\sigma^2 \tag{14}$$

where σ is a constant that is to be estimated and $\frac{1}{6}$ is the weight normalising factor (introduced so that the sum of the weights for the six pore sizes is equal to 1).

The other approach (Case 2) is inspired by the fact that eventually we will apply the calibrated LB model to multi-scaled porous media and therefore we would like to allow that each pore size may contribute differently towards the final error estimate of the LB simulation. For example, smaller pores may be more poorly represented in cell-based discretisations such as those in Figure 5. Also, the rock is a collection of interconnected pores of multiple sizes (Figure 6) and it seems likely that a pore size that appears more frequently might contribute more towards errors in the model result than pore sizes that do not occur so frequently.

Let us consider a simple porous structure: a pipe with diameter 10 and length 100 lattice units. The pore size distribution of this structure consists of

100% of large pores and the permeability of such a structure is very high. On the other hand, consider the same pipe with a planar blockage of thickness 1 lattice unit across the end, but where that blockage has a single hole of width 1 through the middle of it. The pore size distribution by volume now includes 99.9% of large pores and 0.1% of small pores. We have changed the pore size distribution only slightly, but the permeability of the porous medium drops dramatically; the single small pore therefore has an impact on permeability much greater than could be inferred from its representation in the pore size distribution alone. The smaller the cross-sectional area of the small pore, the greater its curbing of permeability. Similarly, in a complex multiscale porous medium, fluid usually flows through multiple passages along any overall flow path and it is the cross-sectional area of the narrowest part of such passages that controls the passage flux.

Given the above physical arguments we expect the uncertainty associated with pores of width w to increase with the number of such pores and to decrease with increasing pore cross-sectional area. We therefore use the following ansatz for the uncertainty contribution from pores of width w:

$$\sigma_w^2 = g(w) = \frac{1}{\sum_w \frac{d(w)}{w^2}} \cdot \frac{d(w)}{w^2} \cdot \sigma^2 \tag{15}$$

where $d(w)$ is the normalised frequency of occurrence of pore size w in the porous medium. The weight normalising factor (first term on the right in Equation (15)) is equal to the reciprocal of the sum of weighting factors $\frac{d(w)}{w^2}$ for all considered pore sizes w.

The pore size frequency distribution is estimated using a publicly available code developed by Bhattacharya et al. [46]. We calculate the effective pore size distribution (the maximum diameter of a spherical particle which fits inside the pore) in lattice units for all eight realisations of different porosity of the Fontainebleau sample (Figure 6) and use the average of the eight curves as $d(w)$. The weights we obtain for pore sizes 3, 4, 5, 6, 7 and 12 are 0.777, 0.133,

0.060, 0.022, 0.007 and 0.0003 respectively. The mismatch between permeability derived theoretically and permeability derived through LB simulation for most values of τ is greater for smaller pore sizes [16] so giving them largest weights will increase the resulting estimate of overall uncertainty of the prediction.

We define the covariance matrices Σ_1 and Σ_2 (the subscripts indicate case number) in Equation (10) to be diagonal matrices containing the entries of Equations (14) and (15) respectively on their diagonals, that is $\Sigma_{1,ii} = \frac{1}{6}\sigma_{w_i}^2$ and $\Sigma_{2,ii} = \frac{1}{\sum_{w_i} \frac{d(w_i)}{w_i^2}} \cdot \frac{d(w_i)}{w_i^2} \cdot \sigma_{w_i}^2$, where entry i on the diagonal corresponds to one of the six pipe widths w_i (3, 4, 5, 6, 7 or 12 lattice units).

4.3. Bayesian formulation for calibration using permeability data (Cases 3 and 4)

Cases 3 and 4 demonstrate Bayesian calibration of the LB model for flow in porous media given experimentally measured permeability data. The data $\underline{D} \equiv \underline{D_{\kappa,E}}$ used in these Case 3 is the porosity-permeability relationship of the Milly la Foret 'normal' Fontainebleau sandstones from [51] (shown in Figures 9 and 10). The covariance matrix Σ_3 that enters the likelihood formulation in Equation (10) then contains several contributions, some of which differ from those in Cases 1 and 2. The first contribution is the experimental uncertainty in the data (σ_{exp}^2): this consists of the uncertainty in the exact permeability of the rock sample given the experimental error involved in measuring permeability $\sigma_{measure}^2$, as well as the effect of anisotropy in the rock which results in differences in permeability depending on the flow direction $\sigma_{anisotropy}^2$ [51]. Our source of experimental data provides only one permeability value per sample and does not explicitly take the direction of flow into account. We make an estimate of this anisotropy uncertainty of 10% of the nominal value of permeability: this is based on LB flow simulations using the three possible cube face pairs of the porous media sample as inflow and outflow boundaries, and comparison of the resulting permeabilities in the three directions.

A further component of the experimental error stems from the fact that, even though Fontainebleau sandstone is fairly homogenous, there is variability

in the measured permeability depending on the sample of the rock that we extract. The variability stems both from the size of samples and from the location of samples in the bigger block of rock. LB simulations in this study are performed on cubic samples of edge length about 1.5mm. The permeability measurements were done on cylindrical plugs with a diameter 40mm and length 40-80mm [51]. There is a discrepancy arising from the smaller scale of the sub-samples in which flow is simulated. We performed a test for sub-sample sizes from 60^3 to 280^3 voxels and confirmed that there is variability in permeability depending on the sub-sample size. The other variability component comes from sub-sample location: different similarly sized sub-samples of a rock sample can have different permeability, even if their porosity happens to be the same or very similar. We combine both of these uncertainties into $\sigma_{rock-sample}$. Since our inference method relies on TMCMC sampling which in turn translates to numerous LB runs, we limit the sample size to control the computational cost to a size of 100^3 for which we estimate $\sigma_{rock-sample}$ of 10% based on our tests.

Similarly to Cases 1 and 2 we have $\sigma^2_{time-sample} \simeq 0$ and the final contribution encompasses the remaining unexplained model error. The overall uncertainty is then:

$$\Sigma_{3,ii} = diag(\sigma^2_{measure,i} + \sigma^2_{anisotropy,i} + \sigma^2_{rock-sample,i} + \sigma^2_{model}). \tag{16}$$

The final term pertaining to the model error is assumed to be constant for all permeabilities.

As an extension to the above, in Case 4 we make a porosity-dependent calibration where we inlude an independent $\tau(\phi_i)$ parameter for LB simulations on samples of different porosities. We couple them using the prediction error equation (8). In order to obtain a mean value and experimental uncertainty for each porosity we bin the measured values from [51] around the chosen porosities, which results in each having multiple measurements. Thus Case 4 augments the number of unknowns to nine, as the relaxation rates are different for each of the eight porosities (6.2, 8.3, 9.8, 11.2, 12.7, 14.4, 16.4 and 21.2 percent). That is,

when data $D \equiv \underline{D_{\kappa,E}}$ is derived experimentally,

$$\underline{D_{\kappa,E}} = \underline{f_\kappa}(\tau_i|M) + \underline{e} \tag{17}$$

where $\underline{e} \sim N(0, \Sigma_4)$, and Σ_4 is defined in (16). The individual relaxation rates per porosity are now coupled via the prediction error $\underline{e}$ through Equation (8).

4.4. Priors on τ and σ

Regarding the priors for the model parameter τ, we assume a uniform prior truncated at bounds $\tau = 0.5$ and $\tau = 1.5$, where the simulation is known to be numerically unstable or computationally impractical. This distribution includes the value of 1.0, routinely used in BGK-LB simulations, as well as the value of 0.857 which is reported by Narvaez et al. [16] to yield the best result of permeability for Poiseuille flow in a quadratic pipe. We also assume uniform priors on σ, truncated at bounds $\sigma = 0.001$ and $\sigma = 10.0$.

4.5. Uncertainty propagation for robust posterior predictions

To obtain the marginal posteriors $p(\tau|\underline{D_{\kappa,A}})$ in Cases 1 and 2 and $p(\tau|\underline{D_{\kappa,E}})$ in Cases 3 and 4 we marginalise the joint posterior of the physical parameter τ with respect to the prediction error parameters. The marginalisation integrals are performed using kernel density estimates of the posterior samples, as produced from the last stage of the TMCMC algorithm [28, 29].

Robust posterior prediction of the output quantity of interest Q (in our case it is the permeability κ) is obtained by taking into account the posterior uncertainties in the model parameters given the measured data D [52]. We define $F_Q(Q|\underline{\theta}, M)$ to be the conditional cumulative distribution of Q given the model parameters $\underline{\theta}$ and the BGK Lattice Boltzmann model M. The posterior estimate is generally formulated as follows [29, 52]

$$\bar{\mu}_Q \approx \frac{1}{N} \sum_{i=1}^{N} \mu_Q \left(\underline{\theta}^{(i)}; M \right) \tag{18}$$

(where N is the number of TMCMC samples) and the posterior variance

$$\bar{\sigma}_Q^2 \approx \frac{1}{N}\sum_{i=1}^{N}\sigma_Q^2(\underline{\theta}^{(i)};M) + \frac{1}{N}\sum_{i=1}^{N}\left[\mu_Q(\underline{\theta}^{(i)};M) - \bar{\mu}_Q\right]^2 \tag{19}$$

of the output Q, where $\underline{\theta}^{(i)}$ are taken from the posterior distribution of $\underline{\theta}$ given D. The posterior PDF in (6), the posterior mean in (18) and the posterior variance in (19) constitute robust measures of uncertainty of Q given the models and the data, taking into account the modelling and parametric uncertainties. The coefficient of variation $COV(Q)$, defined as the ratio of the standard deviation $\bar{\sigma}_Q$ to the posterior mean value $\bar{\mu}_Q$, constitutes an alternative measure of the uncertainty in Q.

5. Results

In Table 2 we summarise the three inference campaigns and some computational details. Each of the four TMCMC sampling campaigns had a significant computational cost. Each LB simulation for the eight samples that occurs in the posterior formulation has a time to solution of around 2 hours running on 64 cores. In order to make the sampling campaign feasible, a significant portion of the κ predictions was replaced by Kriging meta-models using the ideas described in [29]. We ran simulations for several values of parameter τ for each sample and due to the smoothness of the $\kappa(\tau)$ curves (Figure 7) we were able to estimate the permeability prediction for τ values in-between the simulations we ran. This resulted in a substantial reduction in the computational cost (by 92%).

5.1. Uncertainty quantification and propagation using HP (Cases 1 and 2)

In Cases 1 and 2 we use the theoretical formulation of the HP flow through a narrow pipe to infer the posterior PDF of the τ parameter of LB, and we propagate this uncertainty to permeability predictions. We use 5000 samples per TMCMC stage, for a total of 30000 samples, following six stages until convergence.

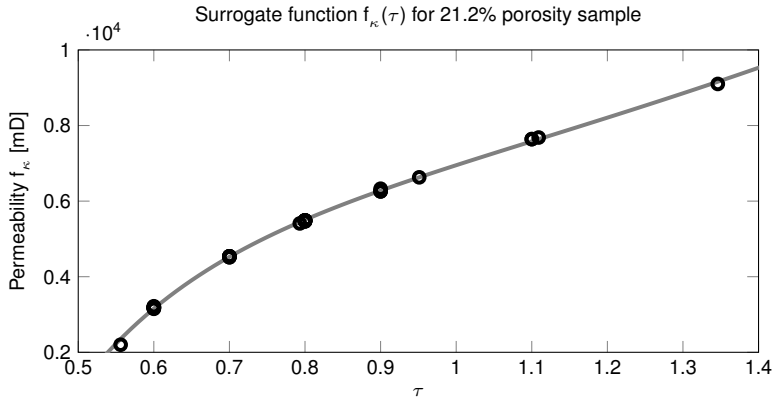

Figure 7: The circles represent the LB runs we performed for the sample of porosity 21.2% and the grey curve represents the best fit to the points that we have used as a surrogate meta-model to predict permeabilities of this sample for a large number of τ values without the computational cost of running the LB simulation.

Table 2: Summary of the four Bayesian inference campaigns presented in the results section.

Case	Data Source	Params	TMCMC Samples (N)	CPU-hrs [1]
1	HP permeability	(τ, σ^2)	30,000	120,000
2	HP permeability	(τ, σ_w^2)	30,000	120,000
3	Fontainebleau permeability	(τ, σ^2)	35,000	210,000
4	Fontainebleau permeability	$(\underline{\tau}, \sigma^2)$	35,000	250,000

[1] As recorded in simulations performed using the UK National Supercomputing Service Archer.

To compare the two models we determine the Bayes factor $K = \frac{p(D|M_2)}{p(D|M_1)}$, where $p(D|M_i)$ is the posterior probability of observed data D given model M_i, or model evidence; M_1 is the error model in Case 1 and M_2 is the error model in Case 2. The model evidence in Cases 1 and 2 is 0.72 and 19.48 respectively, which gives a Bayes factor of 27.0 and points to M_2 being significantly more strongly supported by the data than M_1 [21].

The posterior PDF $p(\tau|\underline{D_{\kappa,A}})$ in each case is estimated using kernel density estimates from the 5000 samples of the last sampling stage, and is presented in Figure 8 (solid curves). The most probable value of τ in Case 1 is 0.949 and in

Table 3: Results of τ calibration for the four cases.

Case	Prior τ	Maximum-a-posteriori τ	Posterior mean τ	Coeff. of variation u
1	$C_1 \cdot U(0.5, 1.5)$[1]	0.949	0.947	3.5%
2	$C_2 \cdot U(0.5, 1.5)$	0.906	0.892	7.5%
3	$C_3 \cdot U(0.5, 1.5)$	0.661	0.667	5.3%
4	$C_4 \cdot U(0.5, 1.5)$	$\tau(\phi) = -1.047\phi + 0.804$	multiple	multiple

[1] C_1, C_2, C_3 and C_4 are normalising constants.

Case 2 it is 0.906. Both are somewhat higher than the value of 0.857 suggested in the literature [16]. The associated coefficient of variation (standard deviation divided by mean) of τ are 3.5% and 7.5% respectively. The distribution in Case 1 has a well pronounced symmetrical peak and in Case 2 is skewed slightly towards higher values with a tail towards lower values to accommodate predictions of all pore sizes.

Using the final 5000 samples we predict the permeability using Equations (18) and (19). We propagate the results using porous media in Figure 5 in order to test whether the so-calibrated LB model can accurately predict permeability for different porosities. The results for Case 1 are summarised in Figure 9 and for Case 2 in Figure 10.

The predictions of permeability are quite similar for the two HP cases. The 95% and 50% credibility intervals (shaded areas), defined as ranges of values with 95% and 50% probability respectively of the predicted value falling within the interval, are considerably wider in Case 2. This reflects the fact that this model endeavours to capture a range of pore sizes.

Our result in Case 1 suggests that the BGK-LB model cannot quantitatively capture the experimental permeability values. The result in Case 2 suggests that the LB model can capture the experimental permeability only for low

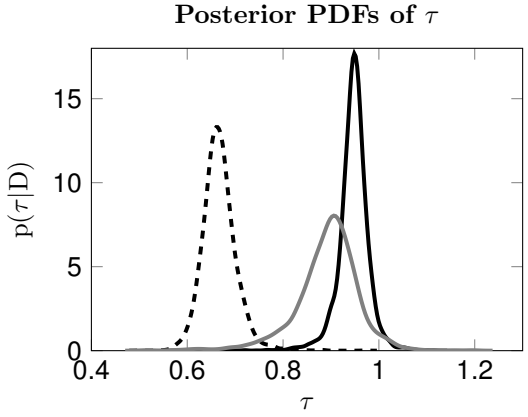

Figure 8: Solid black - calibration using the Hagen-Poiseuille law (Case 1), maximum-a-posteriori (MAP) value at $\hat{\tau} = 0.949$; solid grey - calibration using the Hagen-Poiseuille law using a model that takes pore size and abundance into account (Case 2), MAP value at $\hat{\tau} = 0.906$, dashed - calibration using permeability data (Case 3), MAP value at $\hat{\tau} = 0.661$.

porosities (< 0.12). For higher values predicted permeability lies well outside of the 95% credibility interval, demonstrating the model deficiency in this porosity regime. This over-estimation of the permeability in the LB simulation for even these relatively simple naturally porous sandstones is alarming, as it throws into question the method's applicability to realistic media.

5.2. Uncertainty quantification and propagation using permeability data

In order to reconcile the prediction and experimental discrepancy, we proceed to calibrate our LB model parameter with experimental permeability data.

5.2.1. Porosity-independent relaxation parameter (Case 3)

We again employ the TMCMC with 5000 samples per stage, for a total of 35000 samples, following seven stages until the convergence criteria have been satisfied.

The posterior PDF $p(\tau|\kappa)$ is estimated using kernel density estimates from the 5000 samples of the last sampling stage, and is presented in Figure 8 (dashed curve). A comparison between the three posterior PDFs in Cases 1, 2 and 3 in Figure 8 indicates that the PDF in Case 3 is almost disjoint from the PDFs in Cases 1 and 2. The mode of the posterior PDF using the permeability

information is at $\tau = 0.661$, whereas its associated uncertainty is smaller at 5.3%. This significantly smaller than the value of 1.0 typically used in BGK-LB simulations.

Propagation of the TMCMC samples with the calibrated τ value yields results presented in Figure 11. It is clear that our prediction is significantly better compared to Case 1 or Case 2. We capture a greater range of porosities within the modelling uncertainty. We can predict values with porosities larger than 0.16 compared to 0.12 in Cases 1 or 2. For larger values of porosity, however, we still do not manage to recreate the experimental observations.

The large difference in the predicted values of τ in the HP cases (1 and 2) and Case 3, as well as the persisting discrepancy for over-estimating the permeability for higher-porosity samples, suggests the need to refine the LB model to allow for porosity-dependent relaxation rates.

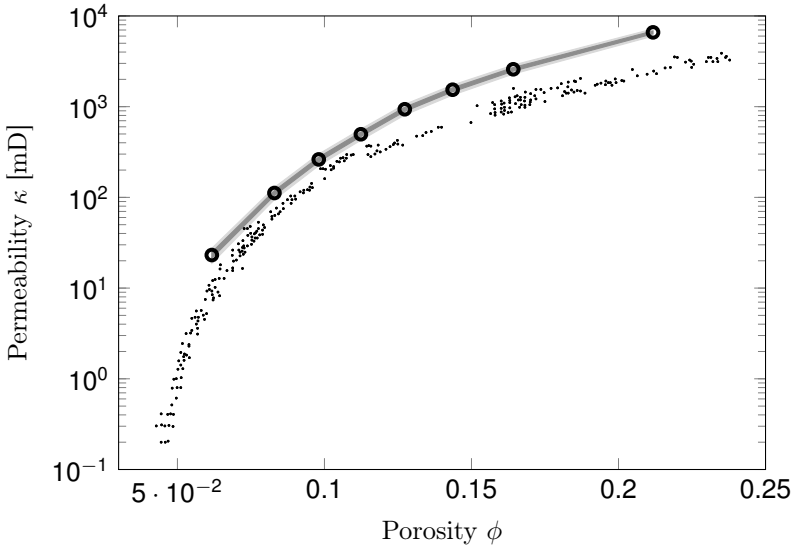

Figure 9: Prediction using the Hagen-Poiseuille law calibration (Case 1). Small dots - experimental data of the permeability of Fontainebleau sandstone ($\underline{D_{\kappa,E}}$) from [51]; light and dark grey shading - 50% and 95% Bayesian credibility intervals; large circles - permeability predictions $\underline{f_\kappa}$ using the MAP $\hat{\tau}$.

5.2.2. Porosity-dependent relaxation rate (Case 4)

We repeat the sampling campaign in order to estimate the posterior distribution function of $p(\underline{\tau}|\kappa)$, where now we allow for the relaxation rates to be porosity dependent. We split the data into eight disjoint regimes of porosity, where we assume that the prediction error within each regime is the same. The marginal τ distributions for all eight porosities are shown in Figure 12.

Figure 13 shows that the MAP values of $\hat{\tau}_{\phi_i}$ fit well with the experimental data and interestingly in this case there is clearly a long tail in each posterior PDF towards lower permeability values. We also fit these MAP values of τ with a linear function in order to suggest which value of parameter τ should be used in simulations on rocks of porosities that we did not model explicitly. Figure 14 presents the resulting MAP relaxation rates as identified for each porosity.

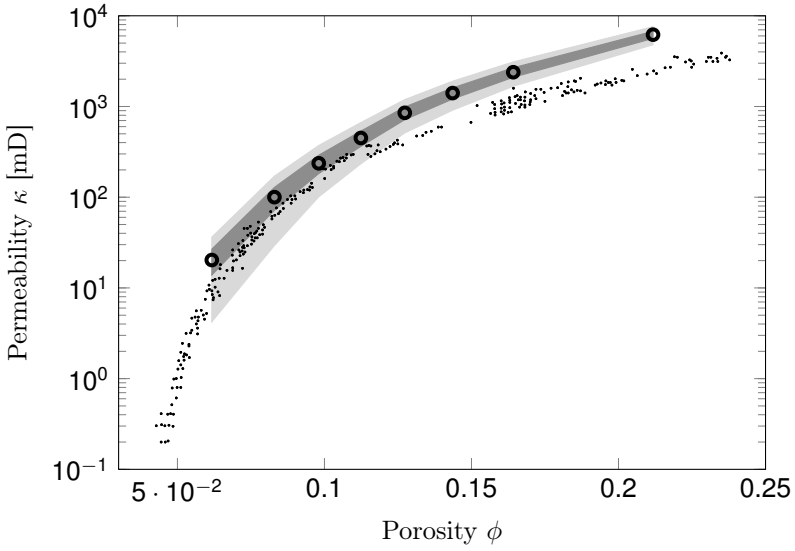

Figure 10: Prediction using the Hagen-Poiseuille law calibration in Case 2. Small dots - experimental data of the permeability of Fontainebleau sandstone ($\underline{D_{\kappa,E}}$) from [51]; light and dark grey shading - 50% and 95% Bayesian credibility intervals; large circles - permeability predictions $\underline{f_\kappa}$ using the MAP $\hat{\tau}$.

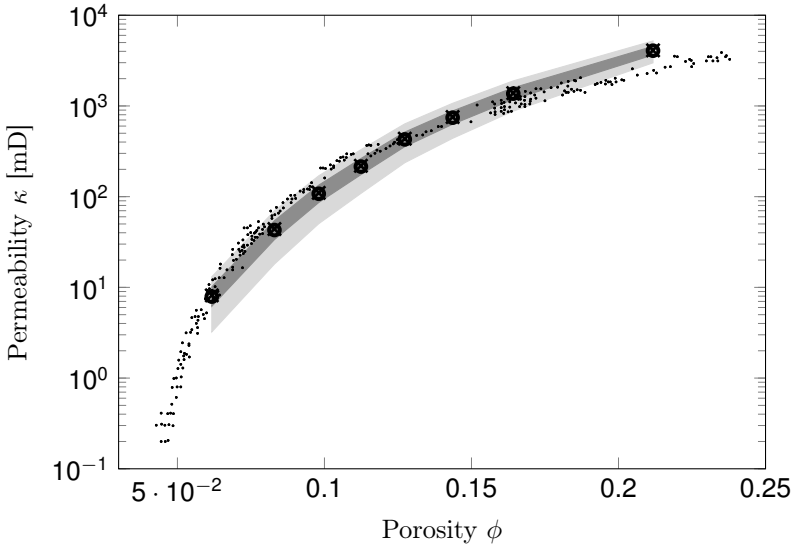

Figure 11: Robust prediction using permeability data (Case 3). Circles indicate predictions using posterior mean τ; crosses indicate predictions using MAP τ; small dots - experimental data of the permeability of Fontainebleau sandstone ($\underline{D_{\kappa,E}}$) from [51]; light and dark grey shading - 50% and 95% Bayesian credibility intervals; large circles - permeability predictions $\underline{f_\kappa}$ using the MAP $\hat{\tau}$.

6. Discussion

Our Bayesian calibration of the BGK-LB parameter τ using permeability data and a porosity-independent formulation (Case 3) results in the MAP value $\tau = 0.661$. This value is considerably smaller than the value found when using the Hagen-Poiseuille law for calibration, and it leads to significantly more accurate permeability predictions (Figure 11). This value, however, is close to the value of $\tau = 0.688$, which is reported by Narvaez et al. [16] as resulting in permeability values that are in good agreement with experimental data for Fontainebleau sandstone. Routine calibration of LB parameters in the literature to-date have depended upon theoretical values for channel flow or similar theoretical cases that are used as test-beds. Results of such calibration fail to predict the experimental values of permeabilities in porous media, even under uncertainty. In the case of a Hagen-Poiseuille calibration the estimated posterior PDF of τ is of limited value for predicting permeability values. This is

due to the different nature of the geometry and flow inside porous media, containing contributions from a range of pore sizes and their complex patterns of interconnections.

When we calibrate τ using all permeability data in a porosity-independent mode (Case 3) the permeability predictions improve overall, but still contain significant discrepancies for samples of higher porosities. This inspired us to assume a porosity-dependent mathematical formulation for the relaxation parameter τ (Case 4). This calibration yields a result where the MAP parameter τ is approximately a function of the total porosity ϕ of a complex medium: $\tau(\phi) = -1.047 \cdot \phi + 0.804$ (Figure 14). This new semi-empirical model for choosing the time relaxation parameter provides significantly more accurate predictions (Figure 13) compared to the porosity-independent case (Figure 11). The superiority of porosity-dependent calibration can be quantified by using Bayesian model prediction and the Bayes ratio between the porosity-independent model evidence and porosity-dependent model evidence in the permeability-based calibration of

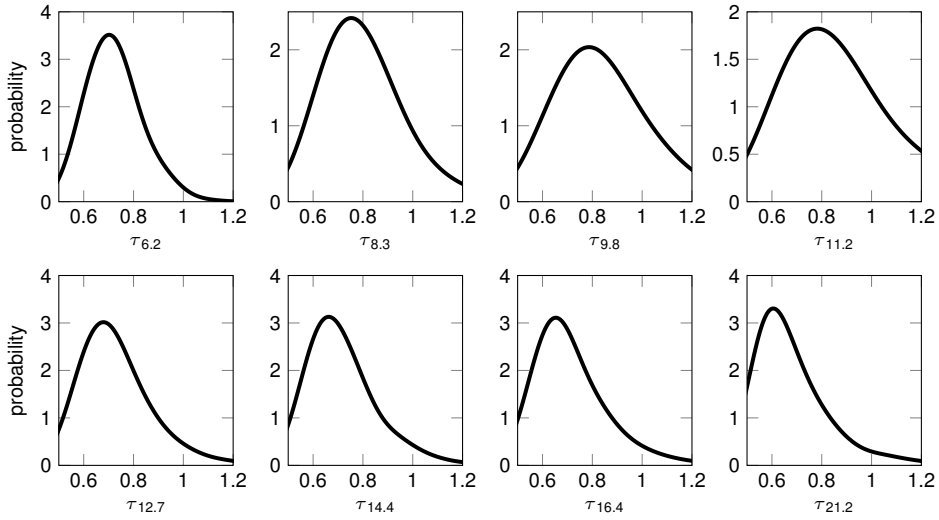

Figure 12: Inference of τ from permeability data using the porosity-dependent model (Case 4). Marginals of the joint posterior PDFs for the eight τ parameters for each analysed porosity (6.2% though 21.2%) are obtained via kernel densities.

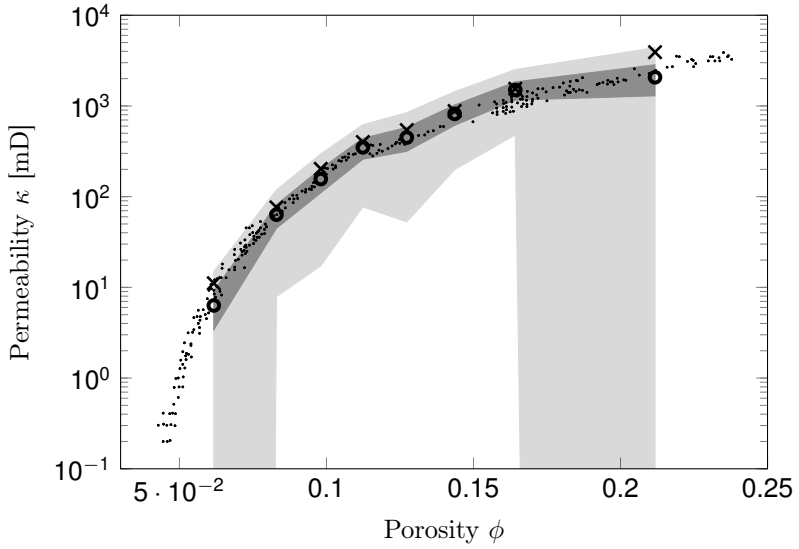

Figure 13: Prediction using permeability data in the porosity-dependent mode (Case 4). Circles indicate predictions using posterior mean τ; crosses indicate predictions using MAP τ; small dots - experimental data of the permeability of Fontainebleau sandstone ($\underline{D_{\kappa,E}}$) from [51]; light and dark grey shading - 50% and 95% Bayesian credibility intervals; large circles - permeability predictions $\underline{f_\kappa}$ using the MAP $\hat{\tau}$.

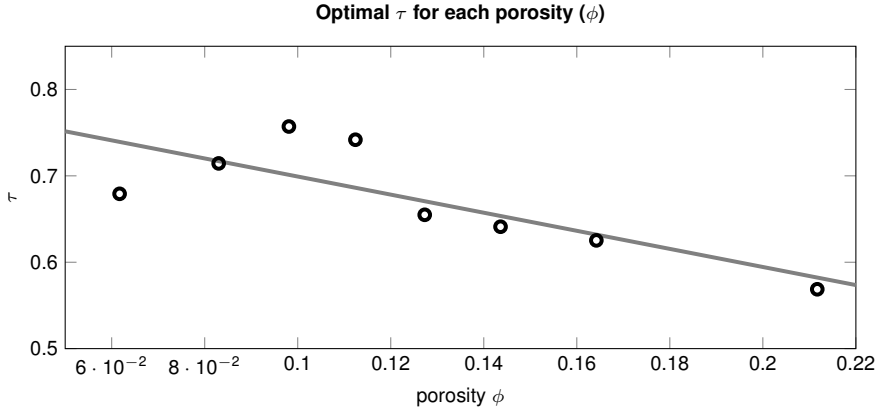

Figure 14: Black circles are the MAP τ for investigated porosities and the grey line is a linear fit of the form $\tau(\phi) = p_1 \cdot \phi + p_2$, where $p_1 = -1.047$, $p_2 = 0.804$.

τ [21]. This ratio is equal to 12.3, which according to Jeffreys [53] is a *strong* evidence that the porosity-dependent model is significantly more plausible given our experimental data.

This empirical model provides a new modus-operandi regarding permeability predictions. To illustrate the predictive power of our model we selected two independent samples of Fontainebleau sandstone. From the collection of microCT images of Fontainebleau sandstone made available by the Institute for Computational Physics of the University of Stuttgart [45] we select two images different from the image used so far: one of resolution $14.6\mu m$ and the other $29.2\mu m$ (Figure 15). Following the procedure detailed in Section 3 we obtain several binary variants of each of the two greyscale microCT images, each with a different porosity: for the $14.6\mu m$ image we generate eight binarisations and for the $29.2\mu m$ image we generate six binarisations (Table 4). We perform two sets of predictions of permeability, one with the value of $\tau = 0.661$ calibrated for the porosity-independent case, and the other using τ according to our semi-empirical model $\tau(\phi) = -1.047 \cdot \phi + 0.804$ (Table 4). The results of the LB simulation for the porosity-independent case (Figure 16) yield permeabilities that fall within the credibility intervals of our propagation for the analysed sample. In the porosity-dependent case (Figure 17) the permeabilities of the independent samples again fall within the credibility intervals, but this time they are also much closer to the experimental data for Fontainebleau sandstone.

Table 4: Parameters τ for the independent samples calculated using the model in Figure 14.

$14.6\mu m$ sample		$29.2\mu m$ sample	
Porosity [%]	τ	Porosity [%]	τ
6.1	0.740	5.3	0.748
8.2	0.718	7.6	0.725
9.6	0.703	10.0	0.699
11.1	0.688	12.6	0.672
12.5	0.673	15.9	0.638
14.2	0.655	20.2	0.593
16.3	0.634		
20.1	0.584		

We would like to stress that LB parameterisation methods, especially for more complex LB models of for example two-phase flows, should be approached with great caution. Depending on the quantity of interest and the experimental set-up we want to simulate, we must carefully assess the relevance of previously published values from literature. Here we present a study for a rock type with published experimental permeability data. In the absence of data for a specific rock formation we suggest that porosity-permeability data at least from a similar rock-type are used. A more involved hierarchical Bayesian approach to calibration involving different types of rocks and theoretical expressions could also be advantageous in this LB calibration method.

Our findings also have significant ramifications for more advanced LB models, including multi-phase, multi-species examples. The usual method of calibration in those systems includes experimental set-ups using contact angle simulations. In future work we will investigate how this calibration compares to calibration with real relative permeability data in the above Bayesian framework. We seek to resolve this matter in two-phase LB simulations (oil and water), which is of notable interest to petroleum engineering.

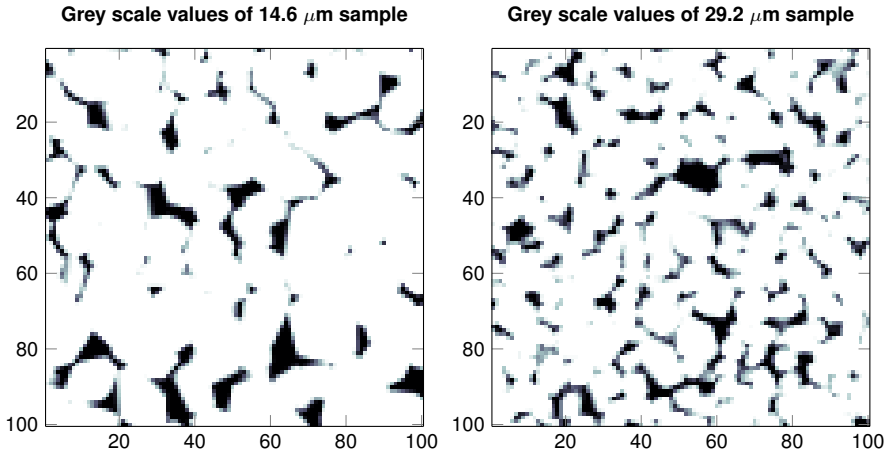

Figure 15: Images of the independent samples used in calibration validation. Slices through microCT image of Fontainebleau sandstone in grey scale.

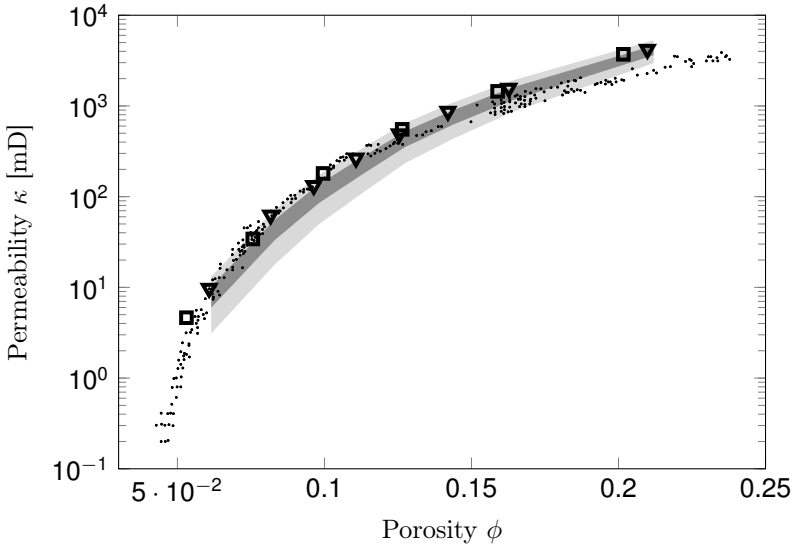

Figure 16: Permeabilities of independent samples calculated using $\tau = 0.661$ in the context of prediction using permeability data (Case 3). Triangles - permeabilities for the $14.6\mu m$ sample; squares - permeabilities of the $29.2\mu m$ sample; small dots - experimental data of the permeability of Fontainebleau sandstone ($\underline{D_{\kappa,E}}$) from [51]; light and dark grey shading - 50% and 95% Bayesian credibility intervals; large circles - permeability predictions $\underline{f_\kappa}$ using the MAP $\hat{\tau}$.

7. Conclusions

We develop a Bayesian inference framework to analyse the power of single-relaxation-time Bhatnagar-Gross-Krook (BGK) Lattice-Boltzmann (LB) models to predict permeability of porous media. The framework enables systematic parameter estimation of LB model parameters (in the scope of this work, the relaxation parameter τ), for the currently used calibrations of LB based on Hagen-Poiseuille law. Our prediction of permeability using the Hagen-Poiseuille calibration suggests that this method for calibration is not optimal and in fact leads to substantial discrepancies with experimental measurements, especially for highly porous complex media.

We proceed to re-calibrate the LB model using permeability data from porous media, which results in a substantially different value of the maximum-a-posteriori (MAP) τ parameter than those proposed previously (0.661 here compared to 1.0 typically used in BGK-LB simulations or 0.857 resulting from

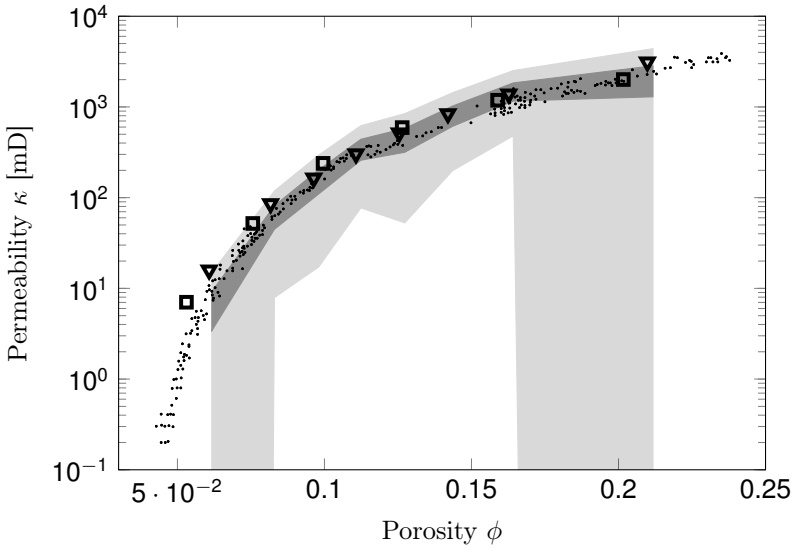

Figure 17: Permeabilities of independent samples calculated using porosity-dependent τ as in Table 4 in the context of prediction using experimental data in the porosity-dependent mode (Case 4). Triangles - permeabilities for the $14.6\mu m$ sample; squares - permeabilities of the $29.2\mu m$ sample; small dots - experimental data of the permeability of Fontainebleau sandstone ($\underline{D_{\kappa,E}}$) from [51]; light and dark grey shading - 50% and 95% Bayesian credibility intervals; large circles - permeability predictions $\underline{f_\kappa}$ using the MAP $\hat{\tau}$.

the calibration for the 3D Poiseuille flow in a quadratic pipe by Narvaez et al. [16]). We augment our model introducing porosity-dependence, where we find that the MAP value for τ decreases for samples of higher porosity. In this new semi-empirical model one first identifies the porosity of the given medium, and on that basis choses an appropriate LB relaxation parameter from the relation in Figure 14. These two approaches result in permeability predictions much closer to the experimental permeability data, with the porosity-dependent case being the better of the two. Validation of this calibration method with independent samples of the same rock type yields permeability predictions that fall close to the experimental data (Figure 16), and again the porosity-dependent model provides better results (Figure 17). We thus conclude that our calibration model is a powerful tool for accurate prediction of complex porous media permeability.

Note that the optimal (MAP) τ is adjusted specifically for the pore ge-

ometries and size distribution of Fontainebleau sandstone. Rock types with a significantly different pore space character should undergo an adjustment of their own.

Finally, the results of this work do not promote the use of BGK-LB over more advanced Multiple Relaxation Time (MRT) scheme, we merely present a state-of-the-art calibration method and showcase the instability of the LB relaxation parameter in the BGK collision model, which is of high importance for any future users of the BGK-LB scheme and should be taken into account in the decision making process of the user.

8. Acknowledgements

We are grateful to Petrobras and BG Group for financial support of the International Centre for Carbonate Reservoirs (ICCR). We acknowledge computational time from the UK National Supercomputing Service Archer, under project number e417.

References

[1] S. Chen, G. D. Doolen, Lattice Boltzmann Method for Fluid Flows, Annual Review of Fluid Mechanics 30 (1) (1998) 329–364.
URL http://arjournals.annualreviews.org/doi/abs/10.1146%2Fannurev.fluid.30.1.329

[2] X. Zhang, A. G. Bengough, J. W. Crawford, I. M. Young, A lattice BGK model for advection and anisotropic dispersion equation, Advances in Water Resources 25 (1) (2002) 1 – 8. doi:10.1016/S0309-1708(01)00047-1.
URL http://www.sciencedirect.com/science/article/pii/S0309170801000471

[3] J. Ma, K. Wu, Z. Jiang, G. D. Couples, SHIFT: An implementation for lattice Boltzmann simulation in low-porosity porous media, Physical Review

E 81 (2010) 056702. doi:10.1103/PhysRevE.81.056702.
URL http://link.aps.org/doi/10.1103/PhysRevE.81.056702

[4] Q. Kang, P. C. Lichtner, D. R. Janecky, Lattice Boltzmann Method for Reacting Flows in Porous Media, Advances in Applied Mathematics and Mechanics 2 (5) (2010) 545–563. doi:{10.4208/aamm.10-10S02}.

[5] A. J. Grodzinsky, Fields, Forces, and Flows in Biological Systems, 1st Edition, Garland Science, 2011.

[6] F. de Monte, G. Pontrelli, S. Becker, Chapter 3 - drug release in biological tissues, in: S. M. Becker, A. V. Kuznetsov (Eds.), Transport in Biological Media, Elsevier, Boston, 2013, pp. 59 – 118. doi:http://dx.doi.org/10.1016/B978-0-12-415824-5.00003-5.
URL http://www.sciencedirect.com/science/article/pii/B9780124158245000035

[7] A.-R. Khaled, K. Vafai, The role of porous media in modeling flow and heat transfer in biological tissues, International Journal of Heat and Mass Transfer 46 (26) (2003) 4989 – 5003. doi:http://dx.doi.org/10.1016/S0017-9310(03)00301-6.
URL http://www.sciencedirect.com/science/article/pii/S0017931003003016

[8] B. A. H. Lorna J. Gibson, Michael F. Ashby, Cellular Materials in Nature and Medicine, Cambridge University Press, 2010.

[9] C. Sun, R. Jain, L. Munn, Non-uniform plasma leakage affects local hematocrit and blood flow: Implications for inflammation and tumor perfusion, Annals of Biomedical Engineering 35 (12) (2007) 2121–2129. doi:10.1007/s10439-007-9377-8.
URL http://dx.doi.org/10.1007/s10439-007-9377-8

[10] F. W. S. Patrick A. Domenico, Physical and Chemical Hydrogeology, 2nd Edition, Wiley, 1997.

[11] X. Zhang, L. K. Deeks, A. G. Bengough, J. W. Crawford, I. M. Young, Determination of soil hydraulic conductivity with the lattice Boltzmann method and soil thin-section technique, Journal of Hydrology 306 (1–4) (2005) 59 – 70. doi:http://dx.doi.org/10.1016/j.jhydrol.2004.08.039.
URL http://www.sciencedirect.com/science/article/pii/S0022169404004159

[12] P. Gibson, H. Schreuder-Gibson, D. Rivin, Transport properties of porous membranes based on electrospun nanofibers, Colloids and Surfaces A: Physicochemical and Engineering Aspects 187–188 (0) (2001) 469 – 481. doi:http://dx.doi.org/10.1016/S0927-7757(01)00616-1.
URL http://www.sciencedirect.com/science/article/pii/S0927775701006161

[13] G. S. Beavers, D. D. Joseph, Boundary conditions at a naturally permeable wall, Journal of Fluid Mechanics (30) (1967) 197–207.

[14] M. A. Camargo, P. C. Facin, L. F. Pires, Lattice Boltzmann Method for Evaluating Hydraulic Conductivity of Finite Array of Spheres, The Scientific World Journal 2012 (2012) 8.
URL http://dx.doi.org/10.1100/2012/527618%]527618

[15] A. Ghassemi, A. Pak, Pore scale study of permeability and tortuosity for flow through particulate media using Lattice Boltzmann method, International Journal for Numerical and Analytical Methods in Geomechanics 35 (8) (2011) 886–901. doi:10.1002/nag.932.
URL http://dx.doi.org/10.1002/nag.932

[16] A. Narváez, T. Zauner, F. Raischel, R. Hilfer, J. Harting, Quantitative analysis of numerical estimates for the permeability of porous media from lattice-Boltzmann simulations, Journal of Statistical Mechanics: Theory and Experiment 2010 (11) (2010) P11026.
URL http://stacks.iop.org/1742-5468/2010/i=11/a=P11026

[17] C. Pan, L.-S. Luo, C. T. Miller, An evaluation of lattice boltzmann schemes for porous medium flow simulation, Computers and Fluids 35 (8–9) (2006) 898 – 909. doi:http://dx.doi.org/10.1016/j.compfluid.2005.03.008.
URL http://www.sciencedirect.com/science/article/pii/S0045793005001520

[18] I. Ginzburg, Consistent lattice boltzmann schemes for the brinkman model of porous flow and infinite chapman-enskog expansion, Phys. Rev. E 77 (2008) 066704. doi:10.1103/PhysRevE.77.066704.
URL http://link.aps.org/doi/10.1103/PhysRevE.77.066704

[19] I. Ginzburg, D. d'Humières, A. Kuzmin, Optimal stability of advection-diffusion lattice boltzmann models with two relaxation times for positive/negative equilibrium, Journal of Statistical Physics 139 (6) (2010) 1090–1143. doi:10.1007/s10955-010-9969-9.
URL http://dx.doi.org/10.1007/s10955-010-9969-9

[20] H. Hammou, I. Ginzburg, M. Boulerhcha, Two-relaxation-times lattice boltzmann schemes for solute transport in unsaturated water flow, with a focus on stability, Advances in Water Resources 34 (6) (2011) 779 – 793. doi:http://dx.doi.org/10.1016/j.advwatres.2011.04.008.
URL http://www.sciencedirect.com/science/article/pii/S0309170811000649

[21] J. L. Beck, K. V. Yuen, Model selection using response measurements: Bayesian probabilistic approach, Journal of Engineering Mechanics-ASCE 130 (2) (2004) 192–203.

[22] J. T. Oden, A. Hawkins, S. Prudhomme, General Diffuse Interface Theories and an approach to predictive tumor growth modeling, Mathematical Models and Methods in Applied Sciences 20 (3) (2010) 477–517.

[23] K.-V. Yuen, Bayesian Methods for Structural Dynamics and Civil Engineering, Wiley-Vch Verlag, 2010.

[24] C. Papadimitriou, D.-C. Papadioti, Component mode synthesis techniques for finite element model updating, Computers & Structures 126 (2013) 15–26.

[25] X. Ma, N. Zabaras, A stochastic mixed finite element heterogeneous multiscale method for flow in porous media, Journal of Computational Physics 230 (12) (2011) 4696–4722.

[26] S. H. Cheung, T. A. Oliver, E. E. Prudencio, S. Prudhomme, R. D. Moser, Bayesian uncertainty analysis with applications to turbulence modeling, Reliability Engineering & System Safety 96 (9) (2011) 1137–1149.

[27] P. M. Congedo, P. Colonna, C. Corre, J. A. S. Witteveen, G. Iaccarino, Backward uncertainty propagation method in flow problems: Application to the prediction of rarefaction shock waves, Computer Methods in Applied Mechanics and Engineering 213–216 (2012) 314–326.

[28] J. Ching, Y. C. Chen, Transitional Markov Chain Monte Carlo method for Bayesian model updating, model class selection, and model averaging, Journal or Engineering Mechanics 133 (7) (2007) 816–832.

[29] P. Angelikopoulos, C. Papadimitriou, P. Koumoutsakos, Bayesian Uncertainty Quantication and propagation in molecular dynamics simulations: a high performance computing framework, Journal of Chemical Physics 137 (14) (2012) 144103.

[30] P. E. Hadjidoukas, E. Lappas, V. V. Dimakopoulos, A runtime library for platform-independent task parallelism, in: Parallel, Distributed and Network-Based Processing (PDP), 2012 20th Euromicro International Conference on, IEEE Computer Society, Los Alamitos, CA, USA, 2012, pp. 229–236.

[31] E. S. Boek, M. Venturoli, Lattice-Boltzmann Studies of Fluid Flow in Porous Media with Realistic Rock Geometries, Computers & Mathematics with Applications 59 (7) (2010) 2305–2314. doi:10.1016/j.camwa.2009.

08.063.
URL http://dx.doi.org/10.1016/j.camwa.2009.08.063

[32] R. Hazlett, S. Chen, W. Soll, Wettability and rate effects on immiscible displacement: Lattice Boltzmann simulation in microtomographic images of reservoir rocks, Journal of Petroleum Science and Engineering 20 (3–4) (1998) 167 – 175. doi:http://dx.doi.org/10.1016/S0920-4105(98)00017-5.
URL http://www.sciencedirect.com/science/article/pii/S0920410598000175

[33] M. E. Coles, R. D. Hazlett, E. L. Muegge, K. W. Jones, B. Andrews, B. Dowd, P. Siddons, A. Peskin, P. Spanne, W. E. Soll, Developments in Synchrotron X-Ray Microtomography with Applications to Flow in Porous Media, Society of Petroleum Engineersdoi:10.2118/36531-MS.

[34] F. M. Auzerais, J. Dunsmuir, B. B. Ferréol, N. Martys, J. Olson, T. S. Ramakrishnan, D. H. Rothman, L. M. Schwartz, Transport in sandstone: A study based on three dimensional microtomography, Geophysical Research Letters 23 (7) (1996) 705–708. doi:10.1029/96GL00776.
URL http://dx.doi.org/10.1029/96GL00776

[35] G. Jin, T. W. Patzek, D. B. Silin, Direct prediction of the absolute permeability of unconsolidated and consolidated reservoir rock, Society of Petroleum Engineersdoi:10.2118/90084-MS.

[36] L. Hao, P. Cheng, Pore-scale simulations on relative permeabilities of porous media by lattice Boltzmann method, International Journal of Heat and Mass Transfer 53 (9–10) (2010) 1908 – 1913. doi:http://dx.doi.org/10.1016/j.ijheatmasstransfer.2009.12.066.
URL http://www.sciencedirect.com/science/article/pii/S0017931009007376

[37] Y. Gao, X. Zhang, P. Rama, Y. Liu, R. Chen, H. Ostadi, K. Jiang, Calculating the Anisotropic Permeability of Porous Media Using the Lattice Boltz-

mann Method and X-ray Computed Tomography, Transport in Porous Media 92 (2) (2012) 457–472. doi:10.1007/s11242-011-9914-7.
URL http://dx.doi.org/10.1007/s11242-011-9914-7

[38] T. Ramstad, P.-E. Øren, S. Bakke, Simulation of Two-Phase Flow in Reservoir Rocks Using a Lattice Boltzmann Method, SPE Journaldoi:10.2118/124617-PA.

[39] A. Grader, Y. Mu, J. Toelke, C. Baldwin, Q. Fang, G. Carpio, B. A. Stenger, T. Al-Dayyani, M. Z. Kalam, Estimation Of Relative Permeability Using The Lattice Boltzmann Method For Fluid Flows, Thamama Formation, Abu Dhabi, SPE Journaldoi:10.2118/138591-MS.

[40] N. Jeong, Advanced Study About the Permeability for Micro-Porous Structures Using the Lattice Boltzmann Method, Transport in Porous Media 83 (2) (2010) 271–288. doi:10.1007/s11242-009-9438-6.
URL http://dx.doi.org/10.1007/s11242-009-9438-6

[41] J. White, R. Borja, J. Fredrich, Calculating the effective permeability of sandstone with multiscale lattice Boltzmann/finite element simulations, Acta Geotechnica 1 (4) (2006) 195–209. doi:10.1007/s11440-006-0018-4.
URL http://dx.doi.org/10.1007/s11440-006-0018-4

[42] B. Ferréol, D. Rothman, Lattice-Boltzmann simulations of flow through Fontainebleau sandstone, Transport in Porous Media 20 (1-2) (1995) 3–20. doi:10.1007/BF00616923.
URL http://dx.doi.org/10.1007/BF00616923

[43] M. C. Sukop, D. T. Thorne, Lattice Boltzmann Modeling, An Introduction for Geoscientists and Engineers, Springer, 2006.

[44] E. Breitmoser, J. Chin, C. Dan, F. D. er, S. Frijters, G. Giupponi, N. Gonzalez-Segredo, F. Gunther, J. Harting, M. Harvey, M. Hecht, S. Jha, F. Janoschek, F. Jansen, C. Kunert, M. Lujan, I. Murray, A. Narvaez,

M. Nekovee, A. Porter, F. Raischel, R. Saksena, S. Schmieschek, D. Sinz, M. Venturoli, T. Zauner, LB3D V7: A Parallel Implementation of the Lattice-Boltzmann Method for Simulation of Interacting Amphiphilic Fluids, http://ccs.chem.ucl.ac.uk/lb3d (2012).

[45] R. Hilfer, T. Zauner, High-precision synthetic computed tomography of reconstructed porous media, Physical Review E 84 (2011) 062301. doi:10.1103/PhysRevE.84.062301.
URL http://link.aps.org/doi/10.1103/PhysRevE.84.062301

[46] S. Bhattacharya, K. E. Gubbins, Fast method for computing pore size distributions of model materials, Langmuir 22 (2006) 7726–7731.

[47] J. Beck, L. Katafygiotis, Updating Models and Their Uncertainties. I: Bayesian Statistical Framework, Journal of Engineering Mechanics 124 (4) (1998) 455–461.

[48] L. S. Katafygiotis, J. L. Beck, Updating models and their uncertainties. II: Model identifiability, Journal of Engineering Mechanics-ASCE 124 (4) (1998) 463–467.

[49] A. O'Hagan, C. Buck, A. Daneshkhah, J. Eiser, P. Garthwaite, D. Jenkinson, J. Oakley, T. Rakow, Uncertain Judgements: Eliciting Experts' Probabilities, Wiley, 2006.

[50] A. Curtis, R. Wood, Optimal elicitation of probabilistic information from experts, Geological Society, London, Special Publications 239 (1) (2004) 127–145.

[51] B. Zinszner, F. M. Pellerin, A geoscientist's guide to petrophysics, Editions Technip, Paris, 2007.
URL http://search.library.wisc.edu/catalog/ocn192082762

[52] C. Papadimitriou, J. L. Beck, L. S. Katafygiotis, Updating robust reliability using structural test data, Probabilistic Engineering Mechanics 16 (2) (2001) 103–113.

[53] H. Jeffreys, Theory of Probability, 3rd Edition, Oxford University Press, USA, 1961.